Review

Journal of the Brazilian Chemical Society

https://dx.doi.org/10.21577/0103-5053.20240081

J. Braz. Chem. Soc. **2024**, *35*, 11, e-20240081, 1-18

Property Tuning through Fine Size Control and Hierarchical Nanostructuring of Metal Oxide Nanoparticles Supported in Porous Matrices: a Review

Cristine S. de Oliveira,[a] *Fernando A. Sigoli*[a] *and Italo O. Mazali*[*,a]

[a]*Laboratório de Materiais Funcionais, Instituto de Química, Universidade Estadual de Campinas, 13083-970 Campinas-SP, Brazil*

In the nanoscale, matter presents different properties compared to its bulk counterparts, owing to the considerable increase of the surface/bulk ratio, as well as the occurrence of quantum confinement effects. One method to fine control the growth of nanoparticles, their size and nanostructure is to use metalorganic deposition combined with a porous matrix as host, where pores act as nanoreactors for nanoparticle growth, resulting in chemically integrated systems. In this review, we look at the history and achievements of the chemical method of impregnation-decomposition cycles for the precise size control, property tuning and tailored synthesis of metal oxide nanoparticles. We give an overview of the various oxide nanoparticles and nanomaterials developed over the years, and how the method of impregnation-decomposition cycles allowed the synthesis of pure, doped and core-shell oxide nanoparticles, as well as the tuning of their properties through the combined fine control of nanoparticle size, nanostructure, and composition.

Keywords: porous materials, nanoparticles, impregnation-decomposition cycles, core-shell, integrated chemical systems

1. Introduction

To this day nanomaterials remain in the highlight of numerous technological advances. Comprised of matter with an average size in the range of 1-100 nm, these small materials have found applications in several facets of science and life, for example in catalysis,[1,2] biomedicine,[3,4] sensors,[5] textiles,[6] energy[7-9] and environmental applications.[10,11] Their wide range of applications stem from the special properties presented by matter in the nanoscale. Compared to their bulk counterparts, nanomaterials have a much larger surface-to-bulk ratio, which means that surface effects become more pronounced. For example, in catalysis, the much higher surface area and/or the higher density of relevant surface defects are advantageous. Other significant effect, observed especially for nanoparticles (NP) below 10 nm, are size-related confinement effects. For semiconductor NP an increase in the band gap is observed, similarly to how plasmons suffer confinement in the case of metallic NP. Both effects may be exploited, for example, to tune the optical absorption or emission profile of the final material for applications in sensing, light-emitting diodes (LED) or photocatalysis. The control of NP size to obtain different light emission profiles was also the research theme of the Chemistry Nobel Prize laureates of 2023, M. G. Bawendi, L. E. Brus and A. Yekimov.[12] Such small nanomaterials, however, typically require some form of stabilization, since their increased and highly energetic surface area is typically unstable and may result in their growth through coalescence, Ostwald's ripening or other growth mechanisms, effectively changing the materials' properties in the process.

On the other hand, while many nanomaterials present interesting properties on their own, the fast pace at which technology advances makes necessary the use of ever more complex materials to fulfil increasingly sophisticated requirements for nowadays' applications. This means that, in most cases, different compounds and materials must be combined to obtain the specific properties required. This aspect, together with the necessity of NP stabilization, infer that a system consisting of NP and stabilizers could be one such complex material. Going a step further, one may also combine NP with functional stabilizers, where both parts of the system have their own unique and equally relevant properties for a given application, as in the case of NP supported on a functional host for catalysis. When each of

*e-mail: mazali@unicamp.br
Editor handled this article: Célia M. Ronconi (Associate)
"Our tribute to Prof. Oswaldo Luiz Alves for his contribution to science, exemplary work, profound wisdom, and unwavering determination."

the individual species, compounds or materials involved perform specific relevant roles for a given application, the complete system may be considered a chemically integrated system.[13-17] New properties may arise of the specific combinations utilized, further enhancing the integration aspect of the system. As an example, a porous material with a functional surface may be used to grow and stabilize NP in its pores, while its pores may function as nanoreactors for localized catalysis performed by NP hosted inside, an aspect that will be further elaborated along the present review.

In this review, we present the synthesis of chemically integrated systems composed by metal oxide NP grown inside porous hosts using the method of impregnation-decomposition cycles (IDC) and the development of this strategy over the past two decades. This method was developed as a layer-by-layer growth strategy to construct such systems based on the combination of a porous material as host matrix with the use of single-source precursors for the bottom-up growth of nanoparticles. The host's pore size, pore network and strong chemical bonds with the grown oxide NP both limit the nanoparticles' growth beyond a certain threshold (given by the pore sizes) and prevent their growth through mechanisms such as coalescence, sintering or Ostwald's ripening. On the other hand, the layered growth allowed control over the amount of metal oxide introduced, the size of the NP, as well as their crystalline phase, morphology and hierarchical nanostructure, allowing to fine tune the oxides' properties by exploiting effects occurring at the nanoscale.

2. The IDC Method: a Layer-by-Layer Growth Strategy

The method of impregnation-decomposition cycles (IDC) was the first application of the typical metal-organic decomposition (MOD) method in confined spaces, by using a porous host as an impregnation matrix.[18] A cycle consists of an impregnation step, where the porous host as either slabs or as powder is immersed in a solution of a specific metalorganic precursor for a set amount of time (typically 8 h) and then washed with a compatible solvent to ensure that the precursor molecules are only inside the porous structure, followed by a decomposition step, where the porous material imbedded with precursor are submitted to thermal decomposition to obtain the desired metal oxide. This process, or cycle, may be repeated at will (Figure 1), with the possibility of changing the precursors used, until the desired nanoparticle structure or size has been reached, or until the porous host can no longer reasonably intake more reagent, due to filled pores and obstructed pore necks, as well as incomplete decomposition resulting of these pore constrictions. This extreme case was observed for a test performed with continuous IDC of ZnO until the impregnation limit of commercially available porous Vycor glass (PVG 7930, or just PVG) was reached at 29 IDC.[20] Another important factor is that, to keep the thermal history of the samples equal, all samples undergo all thermal treatments applied. This means that all samples are thermally treated on every decomposition step, regardless if they undergo impregnation or not, i.e., a sample with 3 IDC and a sample with 10 IDC undergo 10 thermal treatments (from the decomposition steps).

The reagents used to obtain metal oxides are single-source metalorganic precursors, where both the metal and the oxide are provided by the reagent, resulting in the desired metal oxide compound. This reagent may also be combined with smaller amounts (%) of another single-source precursor as a source of a desired dopant for one or more IDC layers. Examples of such reagents are M-2-ethylhexanoates ($M^{x+}(hex)_x$) and M-acetylacetonates ($M^{x+}(acac)_x$).

The next step was then the choice of porous host. From the wide range of materials available at the time, potential candidates had to be chosen based on what the final chemically integrated systems were supposed to achieve: restriction of nanoparticle growth through the porous structure, stabilization of said NP, and chemical

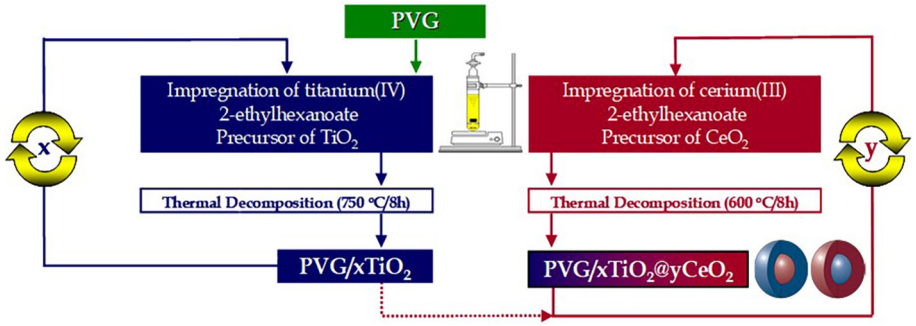

Figure 1. Schematic representation of the impregnation-decomposition cycles (IDC) method, using PVG for the synthesis of either pure TiO_2 or TiO_2@CeO_2 core@shell NP (adapted from reference 19).

and thermal stability against the grown metal oxide NP, as well as to withstand their synthesis and typical application requirements. The first porous host tested was a α-$NbPO_5$ porous glass-ceramic,[18] which presented good chemical and thermal stability, but a large average pore size of ca. 130 nm. The glass-ceramic presented a relatively complex synthesis method, and because of its pore size also resulted in larger NP.[18] The improved properties and either better availability or ease of synthesis, however, quickly brought mesoporous silica glasses such as the PVG and the SBA-15 silica (Santa Barbara Amorphous, or just SBA-15) to the spotlight. With average pore diameter below 30 nm, high chemical and thermal stability, high porosity and high surface reactivity, these porous hosts were promising hosts for the synthesis and stabilization of small metal oxide NP.

The remaining step is the activation of the surface of said porous hosts, optimizing the impregnation of metalorganic compounds. For porous glasses, the composition plays a role as to how these materials should be activated. In the case of the porous silica glass PVG, the most used host for IDC, this is done through two simple steps: the acidic treatment of the PVG slabs with HCl, followed by a treatment with acetone, after which they are stored under vacuum and/or drying conditions before being used. This ensures the availability of active Si–OH sites at the surface, which readily react with the single-source precursors used for metal oxide synthesis. This provides a chemical bond anchoring point for the NP, ensuring their stability within the porous structure and preventing NP coalescence. Furthermore, their thorough distribution throughout the host matrix also prevents other aggregation mechanisms like Ostwalds' ripening. Since such coalescence mechanisms are prevented, the temperature is constant and the concentration of the solution remains approximately constant, NP growth is then governed by the minimization of the high surface/interface free energy of the formed NP,[21] resulting in the desired controlled growth with increasing number of IDC.[22]

3. Typical Characterization Methods

For almost all materials synthesized using IDC a base combination of characterization techniques was used for their structural analysis, and the specifics regarding such IDC-based systems are as follows:

3.1. Cumulative mass gain

The mass gain of the material is linear with the number of IDC, until the impregnation limit of the porous host is reached, corroborating with the controlled growth promoted by the method (Figure 2I).

3.2. N_2 sorption-desorption

Applied to evaluate the pore structure of the host, showing a decrease in available surface area and pore volume with an increasing number of IDC. No change is observed for the curve profiles, proving there is no appreciable clogging of the pore space over as many as 10 IDC (Figure 2II).

3.3. Raman spectroscopy (Raman)

A very powerful analysis technique, given it can measure typical metal oxide vibrational bands as well as those of the porous hosts, where shifts in both wavelength and intensity are meaningful when evaluating the material's properties. This becomes especially important when evaluating which crystalline phases may be present in the structure (this may be either difficult or unreliable through X-ray diffraction or high resolution transmission electron microscopy alone), as well as for the detection and analysis of core@shell structures (Figure 2III), or even for the determination of nanocrystal size using the phonon confinement model.

3.4. Diffuse reflectance spectroscopy in the UV-Vis (DRS)

Considering the porous hosts used present either no absorption or low absorption bands in the low UV-Vis region (200-800 nm), the Kubelka-Munk approximation may be applied on DRS spectra to obtain the metal oxides' characteristic absorption bands within this range, including their band gap (Figure 2IV). Such measurements are indispensable to track the growth of semiconductor oxide NP with the number of IDC, observed by the shift of its band gap due to quantum confinement effects.

3.5. X-ray diffraction (XRD)

The typical XRD profile presents the characteristic glass/amorphous halo of the porous host and generally very broad and low intensity diffraction peaks characteristic of the crystal structure(s) present, and in some cases may only be seen when using a high intensity XRD source. This is a consequence of the very small size of the particles (< 10 nm) and their thorough distribution throughout the porous structure of the host (Figure 2V). Scherrer's law may be applied to obtain an estimate of the average crystallite size, but given the broadening effect the best and most

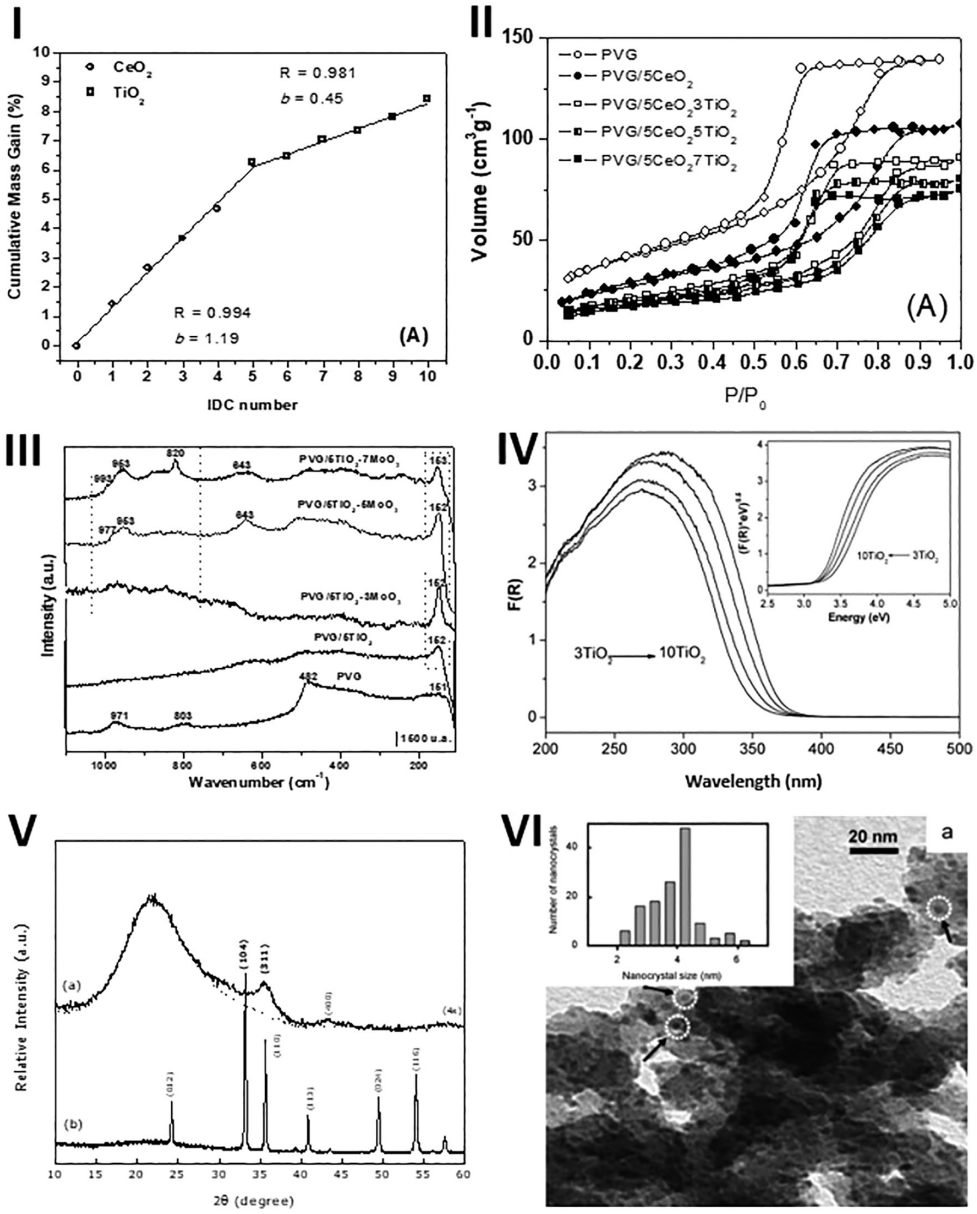

Figure 2. Examples of the typical characterization techniques applied to materials synthesized using the IDC method: (I) cumulative mass gain obtained for the growth of CeO_2@TiO_2 core@shell NP inside PVG (reproduced with permission from reference 19, Copyright 2011, American Chemical Society); (II) N_2 sorption-desorption obtained for PVG/5CeO_2@xTiO_2 (reproduced with permission from reference 19, Copyright 2011, American Chemical Society); (III) Raman spectroscopy measurements of PVG/5TiO_2@xMoO_3 (reproduced from reference 23, Copyright 2010, with permission from Elsevier); (IV) diffuse reflectance spectroscopy (DRS) of PVG/xTiO_2 and respective applied Kubelka-Munk F(R) applied in the inset (reproduced from reference 24, Copyright 2014, with permission from Elsevier); (V) X-ray diffraction (XRD) patterns obtained for free Fe_2O_3 (higher intensity and peak resolution) and PVG/10Fe_2O_3 (reproduced from reference 25, Copyright 2009, with permission from AIP Publishing); (VI) TEM obtained for PVG/7CeO_2, where the inset shows the nanoparticle size distribution obtained for all TEM images collected (reproduced from reference 26, Copyright 2007, with permission from Elsevier).

reliable option for such measurements is through electron microscopy.

3.6. Electron microscopy

Transmission (TEM), high-resolution transmission (HRTEM) and either dark-field TEM or high-angle annular dark-field scanning TEM (HAADF-STEM) are techniques that allow the direct visualization of the NP for evaluation of their morphology, their spread throughout the sample and their size distribution. Through HRTEM or HAADF-STEM one can evaluate the NP crystallinity and possible crystal structure(s) through the diffraction fringes observed. From a series of images (TEM, STEM or HRTEM, depending on the size and visibility of the NP), counting normally at least 200 NP, one can obtain the average size distribution of the synthesized NP (Figure 2VI).

Other techniques such as photoluminescence and magnetic measurements may also contain important structural information, and their individual contributions, both for structural analysis as well as for application tests, will be discussed along this review.

4. Overview of the Metal Oxide Nanoparticle Systems Developed with IDC

A range of different metal oxides and combinations between them was explored, with varying application purposes. From single metal oxides such as TiO_2 and CeO_2 for catalysis, to complex multilayered doped NP for light emitting diode (LED) applications, all systems were planned and tailored seeking to provide a solution to a current challenge at the time of their development. Perhaps the most important properties obtained were the stabilization of very small (< 10 nm) crystalline metal oxide NP inside a porous host, providing micro-chambers, for example, for catalysis, the control of the obtained crystalline phase as well as the fine control of the NP size with varying IDC, both optimizing their chemical activity. In Figure 3, a detailed summary of the metal oxide systems developed using the IDC method is presented, organized according to their composition, main purpose of the work and a short summary of what each work achieved.

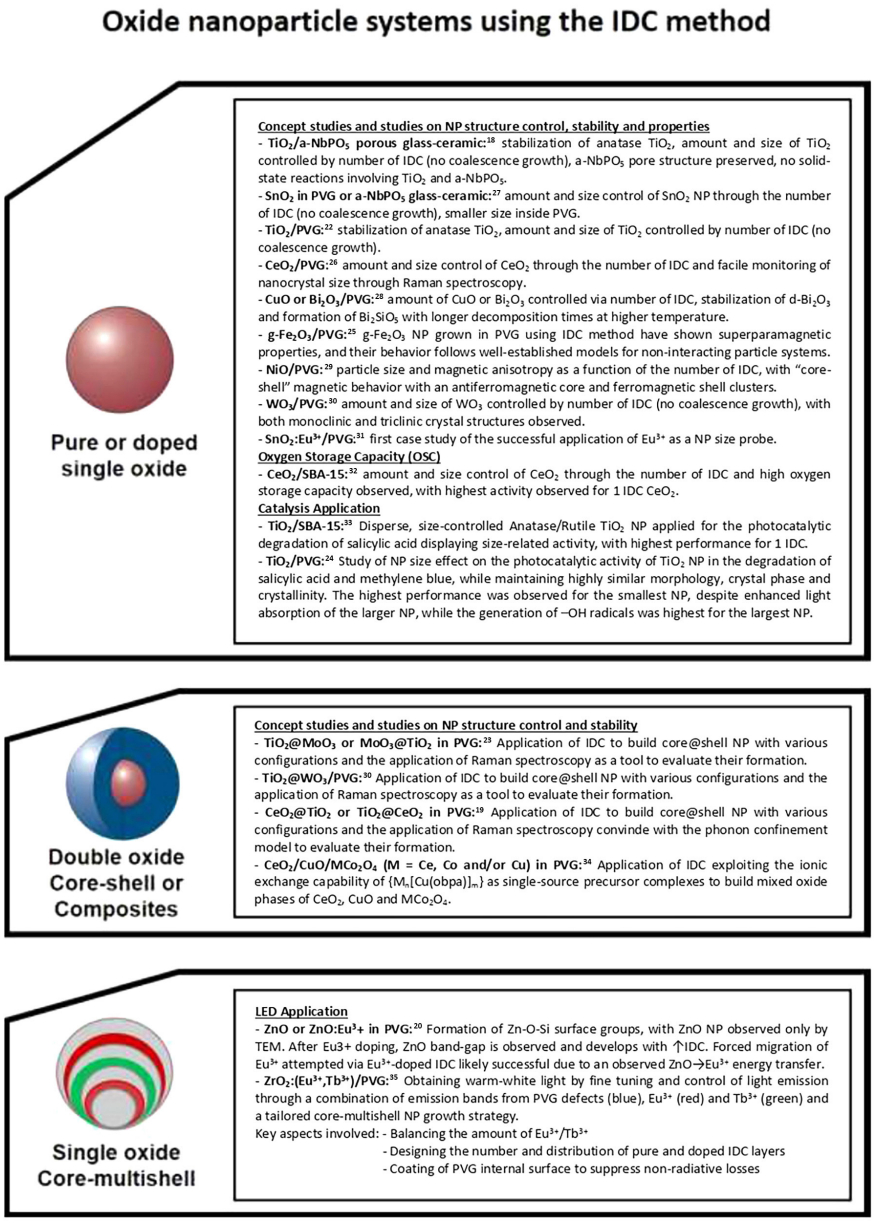

Figure 3. List of the metal oxide systems developed using the IDC related to their composition and/or structure, porous host used, the main purpose of the work and a short description of what each one achieved.

In the following sections each one of the main system categories: single oxide, double-oxide and core@multishell, is discussed in detail.

4.1. Single oxide systems

At first the IDC method was a strategy developed to obtain nanosized metal-oxide inside porous matrices with control over their size and structure, generating materials as chemically integrated systems, where the materials' properties depend not only on the individual composing species, but also on how they interact with each other. The nanoparticles are grown inside the porous host, thoroughly distributed within the porous structure, and they present high crystallinity. The average nanoparticle size is directly proportional to the number of IDC (the higher the number of IDC, the larger the nanoparticles), and presented in general values below 10 nm. A few examples are shown in the TEM images in Figure 4.

The first NP synthesized using this strategy were of TiO_2, an extensively used compound in the fields of catalysis and elimination of environmental pollutants,[36-41]

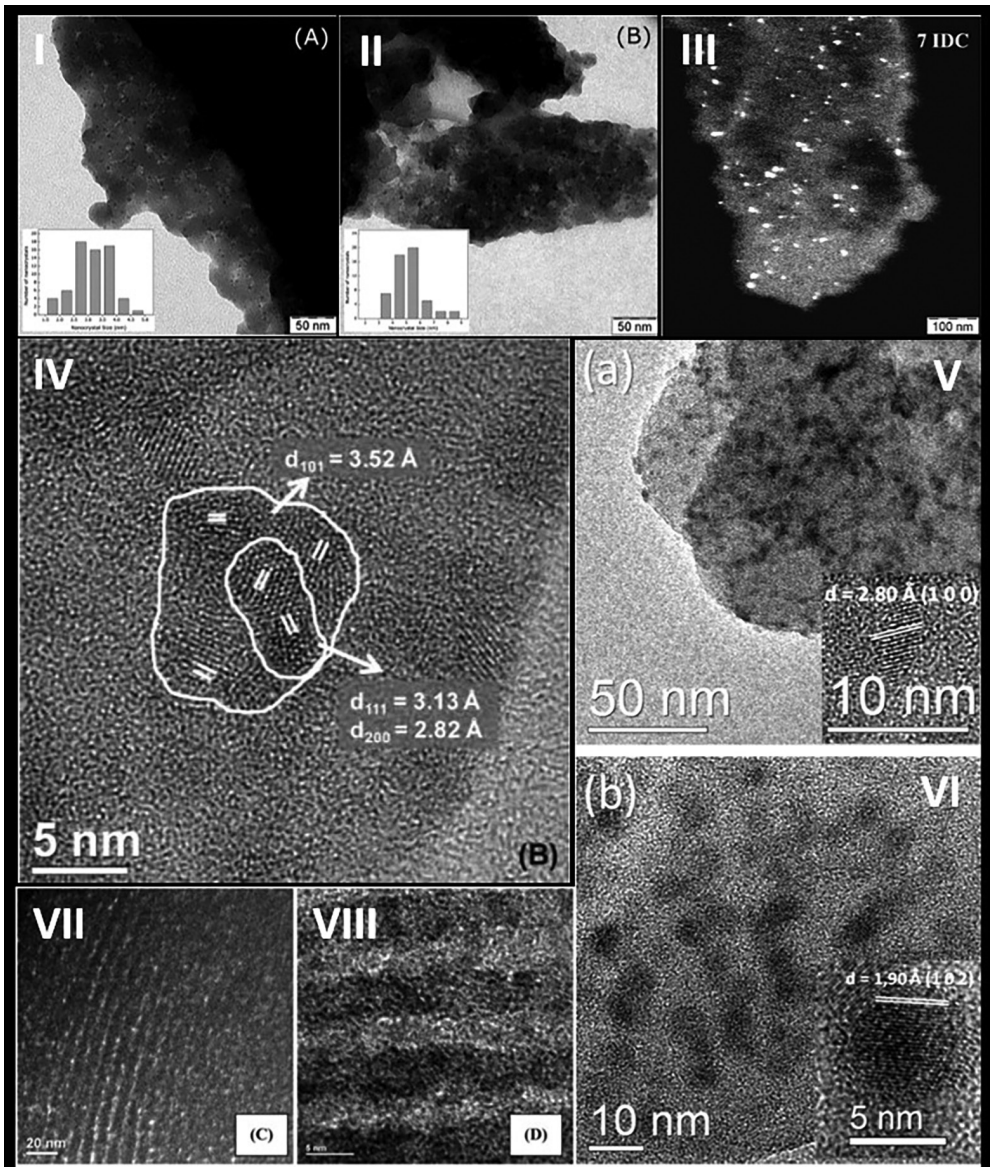

Figure 4. TEM bright field images of γ-Fe_2O_3 obtained with (I) 2 IDC and (II) 8 IDC. The insets show the histograms obtained for the respective particle size distributions (reproduced from reference 25, Copyright 2009, with permission from AIP Publishing); (III) TEM dark field image of NiO NP after 7 IDC (reproduced with permission from reference 29, Copyright 2010, American Chemical Society); (IV) HRTEM images of sample PVG/5CeO_2@15TiO_2 with respective interplanar distances d_{101} = 3.52 Å (anatase TiO_2) and d_{111} = 3.13 Å, d_{200} = 2.82 Å (cubic CeO_2) (reproduced with permission from reference 19, Copyright 2011, American Chemical Society); HRTEM images of samples (V) PVG/10ZnO and (VI) PVG/ZEZ 5/2/10, where the insets show the observed diffraction fringes characteristic of wurtzite ZnO (reproduced with permission from reference 20, Copyright 2015, American Chemical Society); (VII) dark field image and (VIII) HRTEM image of SBA-15/7CeO_2 (reproduced from reference 32, Copyright 2011, with permission from Royal Society of Chemistry).

where the control over size, as well as the stabilization of the TiO_2 anatase crystalline phase, which is normally unstable but much more catalytically active, was made possible.[18] This synthesis was performed in site inside an α-$NbPO_5$ porous glass-ceramic as porous host, previously studied in the group. This first study[18] evaluated all the relevant aspects involved with the method: the impregnation of the metalorganic precursor was confirmed via DRS, and the appropriate decomposition temperature was determined through TGA (thermogravimetric analysis), since the nanoporous environment imposes different conditions on the decomposition process, the process begins more easily since the precursor is well distributed within the matrix, but takes longer to finish because of the pore space restriction, when compared to the free precursor. It was noted that, opposed to the rutile TiO_2 obtained for the free precursor, decomposition performed at up to 750 °C within the porous host resulted in the formation and stabilization of anatase TiO_2 NP, which were well distributed within the porous structure of the host. The cumulative mass gain obtained was linear, which, combined with the analysis of the typical Raman TiO_2 Eg bands for the samples synthesized with increasing number of IDC, have shown that the amount of metal oxide, as well as NP growth are controllable through the number of IDC, and that no sintering or NP coalescence occurs. Furthermore, the porous structure was preserved, and no solid-state reaction was observed between TiO_2 and the α-$NbPO_5$ porous host, given no such characteristic bands were observed through XRD or Raman spectroscopy.

The investigation of such chemically integrated systems then continued with the work by Mazali *et al.*,[27] this time aiming to obtain quantum confined NP using not only the same α-$NbPO_5$ matrix, but also the then commercially available porous Vycor glass 7930 (PVG), which presented higher chemical and thermal resistances, higher porosity and smaller average pore size (< 20 nm). Both SnO_2 and CdS were studied, and we will focus on the results obtained for the former. The crystallite size of the NP was estimated through the Scherrer equation applied to the XRD data, and was smaller for NP synthesized inside PVG compared to α-$NbPO_5$, as would be expected considering the former has a pore size of 4-20 nm, much smaller than the estimated 130 nm of the latter. Furthermore, PVG also presented linear mass increase with the number of IDC, allowing tailored control of the NP size, where no coalescence effects were also observed, owing to the size limitation of the pores in combination with the thorough distribution of the NP over the porous matrix. Lastly, no solid-state reactions were observed. This consolidated PVG as a highly interesting host for such chemically integrated systems, allowing the controlled growth of very small metal oxide NP within nanopores that could present a double function of nanoreactors for catalysis or in gas sensing.

The synthesis of TiO_2 NP was then revisited, this time using PVG as porous host.[22] Once more, anatase TiO_2 was stabilized inside the pores of the host, but this time with a much smaller average size of about 5 nm for 3 IDC. The XRD profile now also presented the glass halo characteristic of PVG together with a broad, lower intensity diffraction peak associated with anatase TiO_2, characteristic of the formation of very small (< 10 nm) NP within a porous host, as mentioned before in this review. Raman spectroscopy analysis of the PVG/xTiO_2 samples corroborate with the phonon confinement model, where the intensity and frequency shift of the TiO_2 E_{2g} mode is a function of the NP size, as can be seen in Figure 5. Nanocrystal growth (related to the Raman band profile) was a linear function of the mass increase alone via IDC, for all samples had the same thermal treatment history regardless of how many impregnation cycles they underwent. This once more proved that the IDC method enabled the tailoring of the NP size, crystalline phase and morphology, and thus of its properties, now within a quantum confinement regime, by using an appropriate porous host.

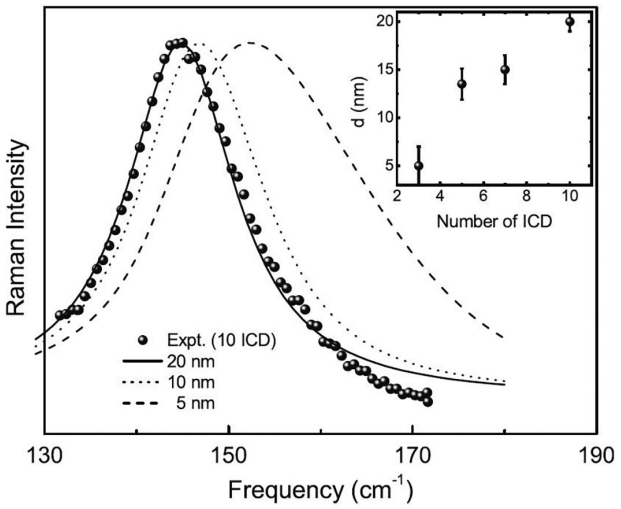

Figure 5. Size-dependent Raman scattering profile of TiO_2 E_{2g} (reproduced from reference 22, Copyright 2006, with permission from Springer Nature). The solid points are experimental data obtained through 10 IDC. The solid, dotted, and hashed lines were obtained by plotting the phonon confinement model equation first formulated by Richter *et al.*[42] for nanocrystal sizes of 20, 10 and 5 nm, respectively. The inset shows the average observed NP diameter obtained through TEM for 3 IDC, and through experimental data fit using the same equation for 5, 7 and 10 IDCs.

The next metal oxide synthesized inside PVG was CeO_2.[26] CeO_2 is a very interesting material especially for catalytic applications,[43-47] where the higher the materials' surface area and better distribution and availability for reacting, the better. It is a natural conclusion then to

synthesize stable and very small CeO_2 NP over large surfaces, especially in a porous host support like PVG, which could in principle be directly used without the need for additional silica added as bedding material. Mazali *et al*.[26] applied the Scherrer's equation to the data obtained through the (220) diffraction peak of CeO_2 for the PVG/xCeO_2 systems, obtaining an estimated crystallite size between 3.7 nm for 3 IDC and 5.6 nm for 10 IDC. TEM images of the PVG/7CeO_2 sample have shown an average NP size of about 4 nm, with a distribution between 2 and 6 nm observed. The Raman spectral signature of CeO_2, the T_{2g} mode at around 460 cm^{-1} undergoes redshift and a decrease in intensity with decreasing IDC. This corroborates with the observed increasing crystallite size with increasing IDC number. A similar fit of the phonon confinement model was performed for CeO_2, where 7 IDC has shown an excellent fit with the theoretical model, and diameters of 3 and 10 nm were obtained for 3 and 10 IDC, respectively. Furthermore, plotting the Raman frequency as a function of the reciprocal nanocrystal size (Figure 6), even combined with results previously obtained in the literature by Spanier *et al*.[48] has resulted in a quadratic dependence of frequency on 1/d, as can be seen in Figure 6. The discrepancies observed between the estimated nanocrystal sizes by TEM, Raman and XRD are a consequence of the different phenomena involved in each. In the case of TEM, what is measured is highly dependent on the resolution, and corresponds to the size of the NP, and not of the crystallites, as is the case for Raman and XRD. The crystallite sizes obtained through these two techniques is also highly dependent on the resolution of the diffractogram or spectrum in question. These in turn are sensitive to the formation and presence of defects or strain in the crystal lattice, ultimately affecting the observed signals and thus the estimated crystallite values obtained.

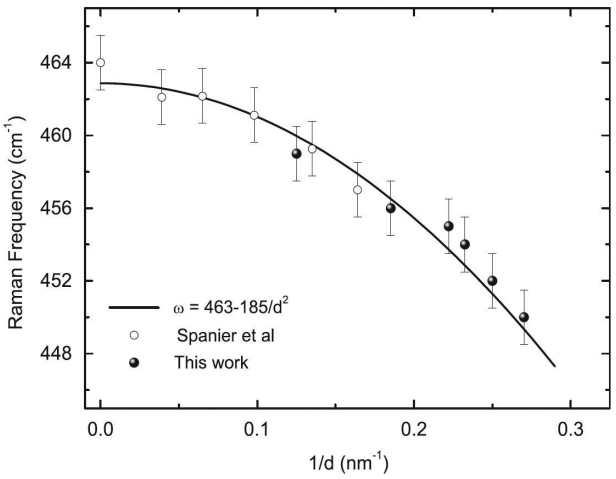

Figure 6. Raman frequency as a function of the reciprocal nanocrystal size (1/d) for CeO_2 nanocrystals, obtained from the work by Spanier *et al*.[48] and the referenced study[26] (reproduced from reference 26, Copyright 2007, with permission from Elsevier).

The synthesis of a PVG/xWO_3 system was also performed, as a part of a larger work seeking the construction of core@shell NP.[30] The latter will be discussed in the respective following section, but a few observations about the pure WO_3 system could be made: as with the previous systems, the mass increment was linear with the number of IDC, indicating control over NP size, but presented a mixture of the monoclinic and triclinic WO_3. Oliveira[28] synthesized other systems such as CuO and Bi_2O_3 in PVG. Both oxides have shown a linear mass increase and, although microscopipc analysis of the samples was not performed, most likely resulted in controlled size of the CuO NP, when one compares the XRD data for PVG/4CuO and PVG/10CuO, for example. Two interesting observations were made for Bi_2O_3, however: first, the stabilized crystalline phase was the normally unstable δ-Bi_2O_3, demonstrating a similar effect of an unexpected phase stabilized in the nanoscale similarly to the observed for TiO_2 NP; second, the cumulative mass gain was almost 4 times higher than for CuO and CeO_2 systems, and with a relatively high decomposition temperature for Bi_2O_3 (600 °C) after 7 IDC the formation of a mixed silicate phase Bi_2SiO_5 was observed. This was the sole example observed for a solid-state reaction involving metal oxide NP grown on silica porous matrices using the IDC method, which in retrospect could be attributed to the high decomposition temperature applied (600 °C), considering the already low melting point of 817 °C for bulk Bi_2O_3.

Another line of research sought the study of magnetic nanoparticles, based on γ-Fe_2O_3[25] and on NiO,[29] both presenting interesting magnetic properties and effects strongly related to the NP size.[49-57] With the size of these materials reduced to the nanoscale regime, surface and finite size effects become prominent and play a pivot role in the nanoparticles' magnetic behavior. Finite size effects correspond to the reduced number of exchange-coupled spins in the particle, while surface effects are related to the lower symmetry at the surface of the NP, generating surface anisotropy and thus magnetic frustration and spin disorder. Such effects may also be enhanced depending on the magnetic behavior of the NP. In the work by Cangussu *et al*.,[25] γ-Fe_2O_3 NP were synthesized in PVG using the IDC method to study the size effect over the properties of the final integrated chemical system. Similarly, to TiO_2, a different crystalline phase was stabilized for the NP in comparison with the expected α-Fe_2O_3 for the bulk structure, and, like in the previous studies, the NP size could be precisely tuned by the number of IDC used. The obtained γ-Fe_2O_3 NP presented magnetic behavior typical

of the expected by well-established non-interacting particle systems, while interacting-particle aspects such as the increasing blocking temperature T_B, the temperature limit above which the system behaves as superparamagnetic, the behavior observed for the NP in question, become more important with an increasing number of IDC as can be seen from the relation between the relaxation time (1/w) at T_B and the inverse T_B in Figure 7. This further corroborates with the well-spread synthesis of the NP within the porous host.

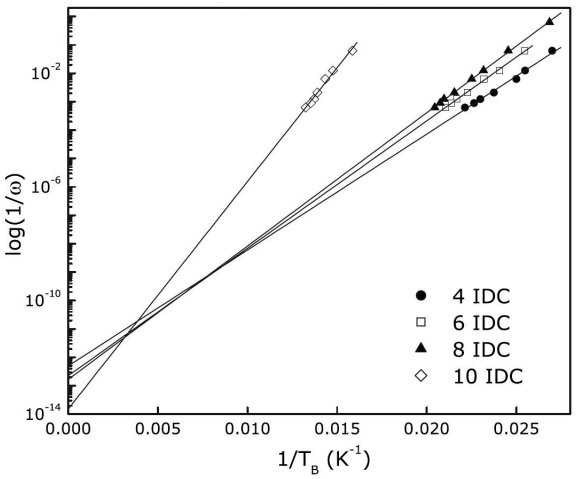

Figure 7. Plot of log (1/w) *vs*. $1/T_B$ for a wide range of measured frequencies of the PVG/x γ-Fe_2O_3 samples, with x = 4, 6, 8 or 10 IDC (reproduced from reference 25, Copyright 2009, with permission from AIP Publishing).

The second work for the synthesis of magnetic metal oxide NP was performed by Carneiro *et al*.[29] with NiO NP in PVG. Once more an increase in the blocking temperature T_B was observed with the number of IDC, as well as a dependance on the magnetic behavior with the number of IDC and thus the size of the nanoparticles. An interesting observation here regarding the magnetic properties measured was the formation of a structure akin to core@shell, composed by an antiferromagnetic ordered core with an uncompensated magnetic moment, coated with magnetically disordered surface clusters. Evidence of this was the intriguing behavior of the field shift hysteresis H_E and the coercivity H_C *vs*. temperature for an increasing number of IDC (Figure 8).

Following a different kind of investigation, this time seeking other means of evaluating the growth of metal oxide NP, Strauss *et al*.[31] were the first to do a systematic study evaluating the potential of investigating the controlled growth of < 10 nm SnO_2 oxide NP by using Eu^{3+} as an indirect luminescence probe. By establishing a relationship between this ion's $^5D_0 \rightarrow {}^7F_1$:$^5D_0 \rightarrow {}^7F_2$ asymmetric ratio and the number of IDC based on Figure 9, they have shown the possibility of using lanthanide luminescence as a highly

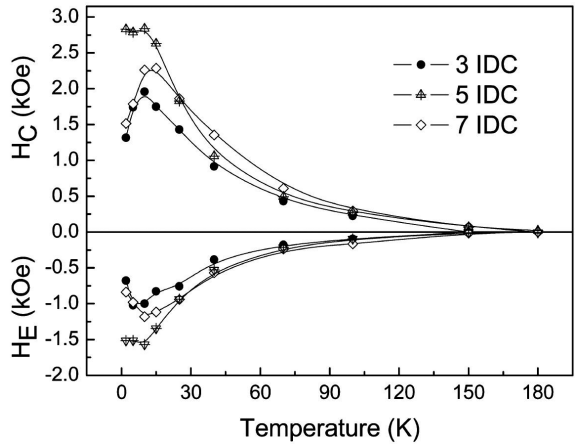

Figure 8. Evolution of the values obtained for the field shift of hysteresis (H_E) and coercivity (H_C) with temperature, for samples with 3, 5 and 7 IDC NiO. The lines serve only as guidance (reproduced with permission from reference 29, Copyright 2010, American Chemical Society).

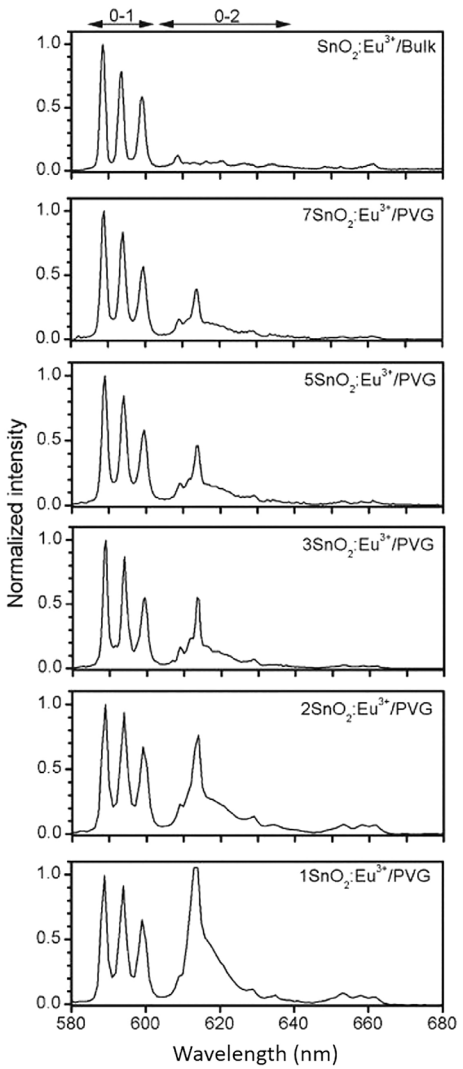

Figure 9. Eu^{3+} emission spectra with l_{exc} = 260 nm obtained for $xSnO_2$:Eu^{3+}/bulk samples where x = number of IDC, and SnO_2:Eu^{3+} bulk sample (reproduced with permission from reference 31, Copyright 2011, American Chemical Society).

sensitive method for nanoparticle size at the quantum confinement regime.

The first work in this research line where an application of such chemically integrated porous host/metal oxide systems was evaluated in addition to the semiconductor properties was in the work by e Silva *et al.*[32] Here, NP of CeO_2 were synthesized inside the pores of an SBA-15 mesoporous silica, and the materials oxygen storage capacity, a very important property regarding metal oxides applied in catalysis, was evaluated *versus* the number of IDC and NP size. This was also the first work in this research line where SBA-15 was used as a porous host for metal oxide NP. The authors have shown it was possible to control the amount of CeO_2 inserted in the system, as well as the size of the CeO_2 NP grown, through the number of IDC, as confirmed *per* XRD and Raman peak/band broadening and shifting, and *per* UV-Vis band gap measurements, with a gradually smaller band gap with an increasing number of IDC, a behavior characteristic of the quantum confinement regime. This corroborates with the observed for the previous systems with PVG as host, as well as with CeO_2 or other oxides. N_2 adsorption-desorption data also corroborated with a lowering surface area and pore volume with an increasing number of IDC. While no blockage of the pore structure was observed, a contraction of the porous host structure was occurring with every IDC, the cause of which was attributed to the thermal treatment of the decomposition step(s), a behavior typically expected for such ordered mesoporous silicas. Furthermore, due to the ordered nature of the porous host, TEM dark field HRTEM measurements were necessary to observe the CeO_2 NP inside the SBA-15 structure. The oxygen storage capacity (OSC) of the SBA-15/xCeO_2 was measured through hydrogen uptake by temperature programmed reduction (H_2-TPR) (Figure 10). One can immediately see the effect of the small size of NP at 1 IDC when compared to the samples with 5 and 10 IDC: the absence of a second H_2 consumption peak. The second peak at higher temperature is a result of bulk CeO_2 reacting with H_2, showing that at 1 IDC the NP size is indeed so small that the "surface" CeO_2 response is the only one observed. With the growth of the NP with 5 and 10 IDC, the second peak then appears, showing the increasing presence of "bulk" effects. One could also infer that the surface CeO_2 is the most reactive, since the normalized uptake of H_2 is much higher for 1 IDC, a justified observation since the smaller the NP, the higher the crystal lattice distortion and thus the higher the resulting oxygen non-stoichiometry.

In a following work using SBA-15, the authors sought to grow TiO_2 NP, similarly to what was done before with PVG, and tested the applicability of the samples

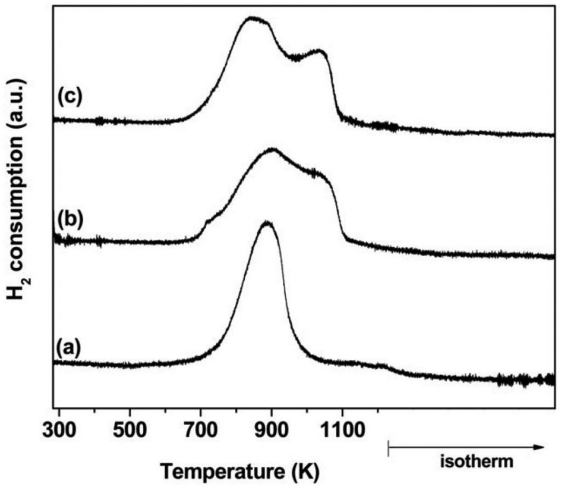

Figure 10. H_2-TPR measurements obtained for SBA-15/xCeO_2 samples, where (a), (b) and (c) correspond to 1, 5 and 10 IDC, respectively (reproduced from reference 32, Copyright 2011, with permission from Royal Society of Chemistry).

in the photocatalytic degradation of salicylic acid.[33] N_2 sorption results corroborated with the observed for the SBA-15/xCeO_2 systems, and the same control of NP size and oxide amount was possible with the number of IDC, but one important difference was observed: the formation of mixed phases of rutile and anatase TiO_2 NP, in contrast to the pure anatase phase obtained when using PVG. Another important difference was observed on the DRS spectra, where the band gap energy was much higher than expected for TiO_2 NP. While the increase in band gap energy is normally expected and attributable to the quantum confinement effect for NP < 5 nm, this abnormal increase was attributed not only to this effect, but to a combination also involving the formation of strong Ti–O–Si bonds. This second effect can strongly modify the electronic structure of the Ti atoms by increasing its effective positive charge, further increasing the band gap energy. One could infer, however, that some other effect related to the difference in porous host might play a role, since PVG also forms Ti–O–Si bonds and this abnormal band gap energy increase is not observed in the case of PVG/xTiO_2 systems. The performance of the synthesized samples in the photocatalytic degradation of salicylic acid has shown that the sample with the smallest size NP and thus also lowest relative amount of TiO_2 presented the highest activity (PVG/1TiO_2) (Figure 11). This result shows that, despite the larger band gap, and thus lower photon absorption rate of the sample, the surface area and surface catalytic performance play a much more important role, which can also be observed by the rather similar performance of the following higher IDC samples. This result also corroborated with the OSC performance of CeO_2 NP, where the sample with 1 IDC has shown the most relative activity.

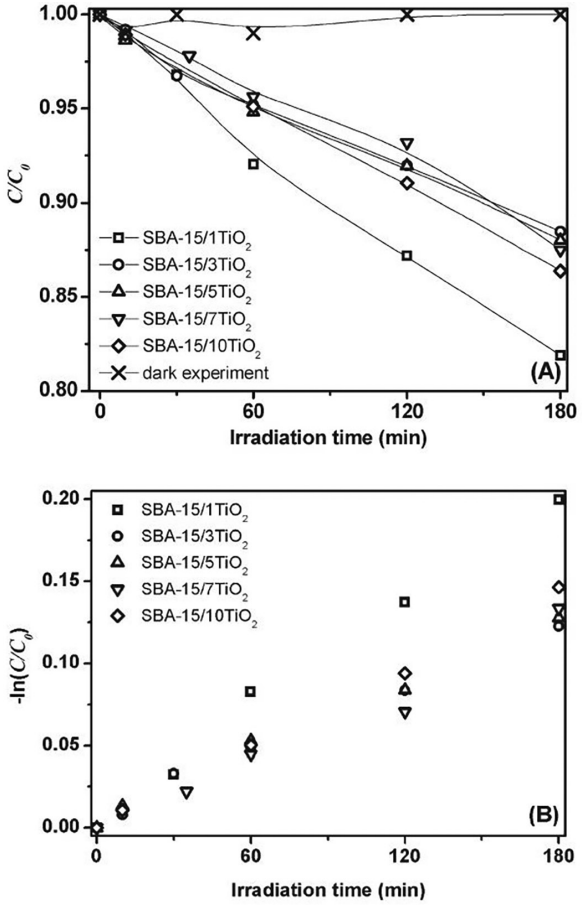

Figure 11. Catalytical performance of SBA-15/xTiO_2 for the photodegradation of salicylic acid, where C is the concentration of acid as a function of time and C_0 is its initial concentration. Through the Langmuir-Hinshelwood model applied to a substrate with low initial concentration, the equation may be simplified to the pseudo-first order expression $-\ln(C/C_0) = kt$, and thus the rate constant k may be determined from a curve of $-\ln(C/C_0)$ *vs.* t (reproduced from reference 33, Copyright 2013, with permission from Royal Society of Chemistry).

The last work in this line of investigating metal oxide NP/porous host chemically integrated systems constructed via IDC for catalytical-related applications was the work by Strauss *et al*.[24] In this work, the authors sought to isolate the size effects from other possible effects affecting TiO_2 NP catalytical performance, and to understand the former in detail through the application of PVG/xTiO_2 systems in the photocatalytic degradation of salicylic acid and methylene blue decolorization. Samples with TiO_2 NP with different sizes obtained through different numbers of IDCs were tested, and similarly to the previous systems an inverse relationship between size and photocatalytic activity was observed, as can be seen in Figure 12. However, the formation of one of the most reactive species involved in photocatalytic oxidation processes, the hydroxyl radical •OH, was observed to be directly proportional to the size of the TiO_2 NP. This is expected, since the generation of these radicals is enhanced with the improved absorption of light by the NP, which gradually increases with gradually smaller band gaps with an increasing NP size. These two aspects (the surface-to-bulk ratio and the formation of hydroxyl radicals) seemed at first at odds against one another, since the photocatalytic activity was highest for the smallest NP, even with the less efficient •OH formation. This has shown that surface effects played a more significant role in the photocatalysis mechanisms involved, with the higher surface area favoring adsorption-desorption mechanisms for the organic compounds studied, and the higher surface-to-bulk ratio reducing the amount of recombination volume ("bulk" TiO_2). Since the recombination of photogenerated electrons and holes occurs mostly in the "bulk", and since this mechanism is the key suppression pathway for the photocatalytic activity of TiO_2, as they are responsible for the formation of strongly oxidizing and reducing species involved in photocatalysis, it makes sense that preventing it by constructing higher surface-to-bulk ratio NP plays the major role in the material's photocatalysis performance.

4.2. Core@shell systems

Through the single metal oxide NP chemically integrated systems described so far it was clear to see how the control of NP growth and thus size, as well as their stabilized crystalline phase through the number of IDC lead to the fine tuning of the material properties. It was also observed that the layer-by-layer growth promoted by this method could create a new degree of complexity in the system by building core@shell NP, exchanging the single-source precursor after a number of IDC to grow a shell of a different metal oxide.

The first attempt was performed by Santos *et al*.[23] through the synthesis of TiO_2@MoO_3 and MoO_3@TiO_2 NP in PVG. The formation and development of the core@shell structure was done through Raman spectroscopy (Figure 13), by monitoring the anatase TiO_2 E_{2g} band at around 150 cm^{-1} and the α-MoO_3 characteristic υ_{sym}Mo=O and corner sharing υMo–O–Mo bands at around 990 and 820 cm^{-1}, respectively. With an increasing number of IDC, a shift to lower energy and higher intensity are observed for both the pure TiO_2 and MoO_3 NP, a characteristic behavior as *per* phonon confinement effect due to the small NP size. With a MoO_3 core, adding subsequent layers of TiO_2 results in the observation of TiO_2 characteristic bands, displaying phonon confinement, while the MoO_3 slowly lose intensity. In the other way around, with a TiO_2 core and a MoO_3 shell, the reverse is observed. This effect was one of the indicators of the formation of a core@shell structure. Furthermore, the broadening of the bands, as well as disappearance or low definition of the corner sharing υMo–O–Mo bands together

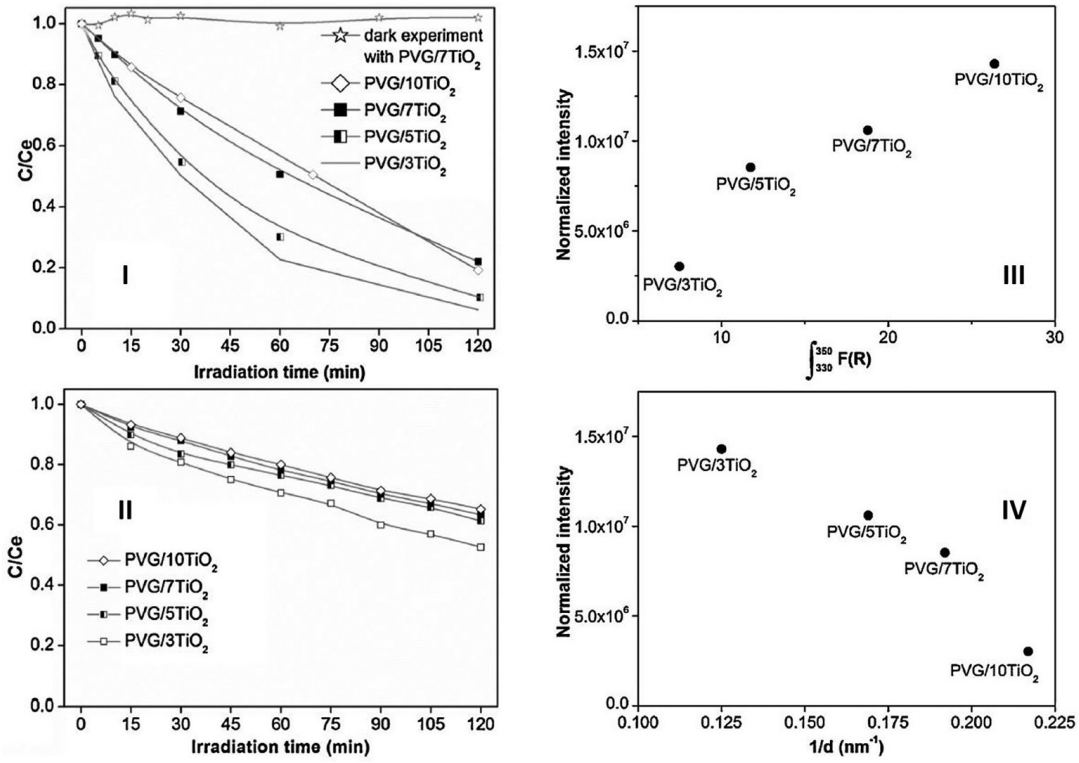

Figure 12. Catalytical performance of PVG/xTiO_2 for (I) salicylic acid photodegradation and (II) methylene blue decolorization. Evaluation of OH radical formation by TiO_2 irradiation through hydroxyl reaction with terephthalic acid (TPA), where (III) relates the normalized intensity of TPAOH emission against the light absorption response and (IV) against the inverse of NP size determined from Raman spectroscopy (reproduced from reference 24, Copyright 2014, with permission from Elsevier).

with the dislocation of the υ_{sym}Mo=O band to lower energies were also remarkable signs of the formation of a core@shell structure, both in the case of coating with a TiO_2 shell and for a thinner shell of MoO_3, resulting of distortions in the corner sharing octahedral structure in MoO_3. Another strong indicator was the phonon confinement effect observed when varying "core" and "shell" thickness: for larger cores with a similar shell size, a stronger confinement was observed, corroborating with an expected thinner shell in the case of core@shell formation. A work[30] reporting the synthesis of TiO_2@WO_3 in PVG soon followed, since a readily dispersion of WO_3 over TiO_2 is expected owing to the strong Ti–O–W bonding. The authors observed the formation of mixed triclinic and monoclinic phases in the case of WO_3, both for the pure core and for WO_3 shells, and similar effects to TiO_2@MoO_3 systems were observed regarding Raman analysis. The direct visualization of the core@shell structure through HRTEM measurements for these samples was not possible, which was attributed to a very thin shell being formed, together with the mixed phase profile of WO_3, and the fact the NP are contained within a porous host, hindering the visualization of diffraction fringes.

The work by Correa *et al.*[19] expanded on the strategy from Santos *et al.*[23,30] for the synthesis of core@shell NP of TiO_2 and CeO_2 in PVG, tuning core and shell sizes not only with fixed core or shell but also simultaneously changing the number of IDC for both, for TiO_2@CeO_2 and CeO_2@TiO_2 systems. The analysis of the TiO_2 E_g and CeO_2 T_{2g} bands in the Raman spectra led to similar conclusions as the observed for the previous core@shell systems, and the observed results also fit very well with the theory of phonon confinement according with the size/thickness of the core/shell analyzed. One important aspect to consider is the different, albeit expected, behaviors of bands E_g and T_{2g} with increasing particle size: E_g is shifted to lower frequencies, while T_{2g} is shifted to higher frequencies, a result of the different phonon dispersion relations for the phonon branch to which each Raman mode belongs. Another interesting observation was the suppression of CeO_2 surface defects when coated with a TiO_2 shell, noted by the absence of defect-related bands in the region of 360 to 480 cm^{-1}, which also become very prominent for very thin CeO_2 shells. The authors also sought to image the core@shell structure of the NP by synthesizing a PVG/5CeO_2@15TiO_2 sample, since with fewer IDC the shell size is too thin to be imaged with the HRTEM used. This attempt proved successful, and an exemplar core@shell NP can be seen on Figure 14.

A study by Kalinke *et al.*[34] followed a different approach, aiming to synthesize mixed oxides and mixed-

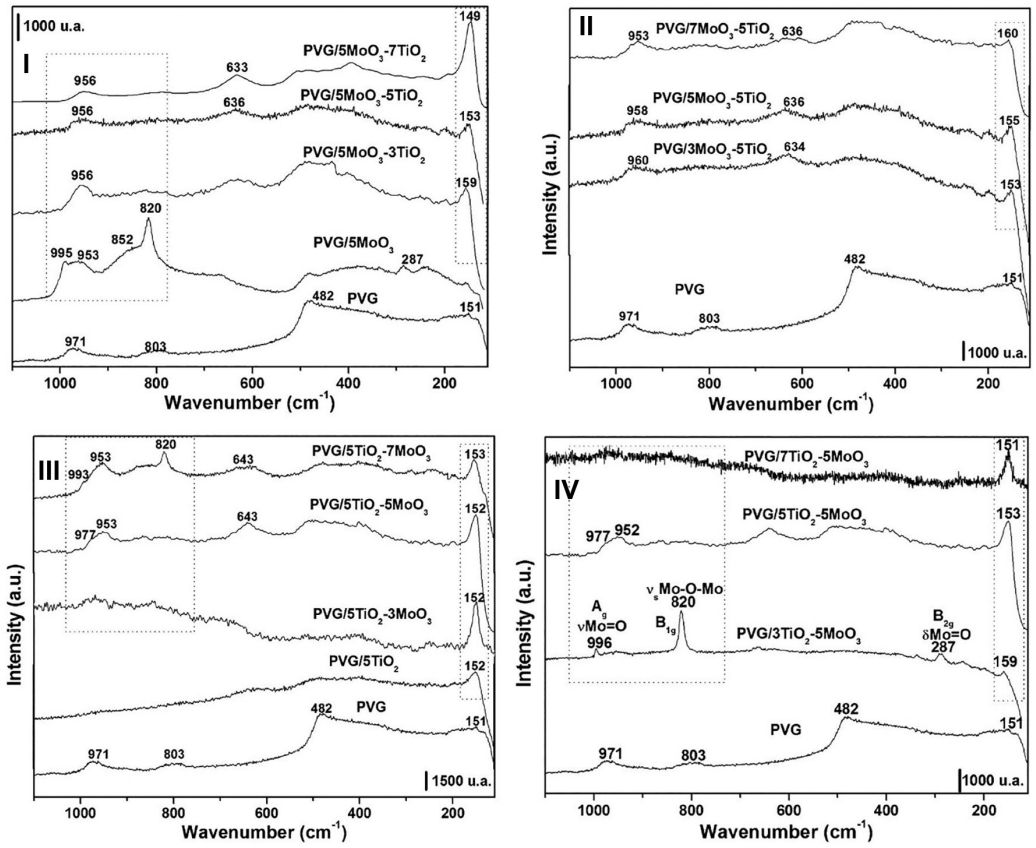

Figure 13. Raman spectra obtained for (I) PVG/5MoO_3@xTiO_2; (II) PVG/xMoO_3@5TiO_2; (III) PVG/5TiO_2@xMoO_3 and (IV) PVG/xTiO_2@5MoO_3, where x = 0, 3, 5 or 7 IDC (reproduced from reference 23, Copyright 2010, with permission from Elsevier).

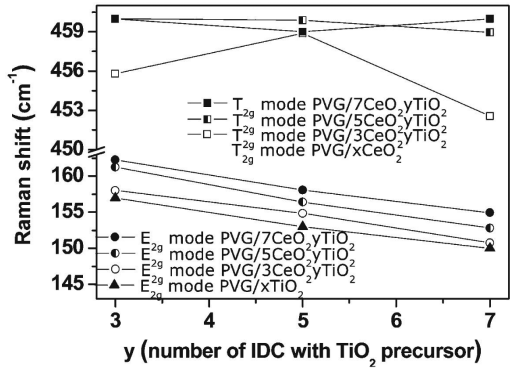

Figure 14. Raman shifts observed for PVG/xCeO_2@yTiO_2, where x and y = 0, 3, 5 or 7 (reproduced with permission from reference 19, Copyright 2011 American Chemical Society).

phase oxides of Cu, Ce and Co using PVG as porous host and bimetallic complexes as single-source precursors, where the impregnation step was performed twice with different metal complexes before the decomposition step. Although partial cation substitution was observed for CuO/CeO_2 systems, these did not form a mixed oxide, but the formation of spinel copper cobaltite ($(Cu,Co)Co_2O_4$) with average size slightly above twice that of the individual oxides was observed (9 nm compared to 4 nm). This study implied the possibility of synthesizing mixed oxides or mixed oxide phase composites with fewer decomposition steps, using specific precursors that would allow the insertion of different metals before the decomposition, where the oxide formation is promoted.

4.3. Core@multishell systems: application-oriented design of hierarchical multilayer nanoparticles

The studies shown so far had demonstrated the IDC method's potential and flexibility in the synthesis of tailored single-oxide and oxide@oxide core@shell and composite nanoparticles. The following studies took this a step further: the application-oriented design of nanoparticles by tailoring their hierarchical multilayer structure.

The first work by Oliveira *et al.*[20] followed that approach by designing single-oxide core@multishell ZnO:Eu^{III} NP in an attempt to incorporate Eu^{III} into the ZnO wurzite crystal structure, a very difficult task considering the much larger size of Eu^{III},[58-64] where the higher concentration of structural defects in NP was considered as a means for the successful doping. The strategy was to induce the forced thermal migration of Eu^{III} by making a "sandwich" structure with Eu^{III}-doped ZnO IDC layers in-between pure ZnO oxide IDC layers. The behavior of ZnO, however, was different

from the expected based on the previous oxide systems. It seemed to interact much more effectively with the surface of SiO_2 than with itself, promoting the formation of Si–O–Zn groups instead of ZnO nanoparticles. A consequence of this was that no ZnO band gap was observed at first (Figure 15), only a shoulder at higher energy (225-250 nm wavelength) attributed to these surface groups, although NP were still observed through TEM. Interestingly, after the addition of the first ZnO:Eu^{III} layers, the formation of the ZnO band gap is then observed with ever increasing and red-shifting intensity with ↑IDC. This has shown that the insertion of a different species has promoted ZnO NP growth, much like a "seeding" process.

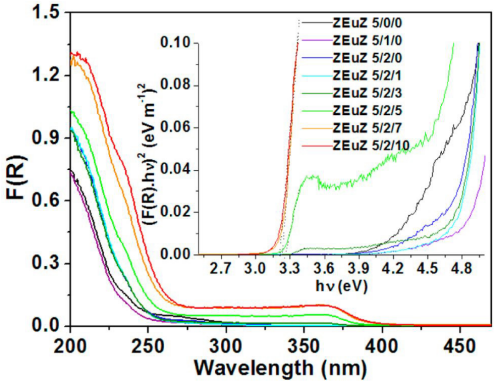

Figure 15. UV-Vis absorption spectra obtained by DRS using the Kubelka-Munk function for PVG/ZnO@ZnO:Eu^{III}@ZnO samples. The inset shows the $(F(R).hv)^2$ *vs*. hn plots (reproduced with permission from reference 20, Copyright 2015, American Chemical Society).

Looking at the photoluminescence curves (Figure 16), the presence of a ZnO → PVG energy transfer, where corresponding ZnO bands are observed when looking at the excitation spectra of a PVG-specific emission band (λ_{em} = 435 nm), corroborates with the strong interaction observed between SiO_2 and ZnO. A clear and definitive sign that Eu^{III} had been successfully inserted into ZnO was not observed, but the presence of "bulges" in the Eu^{III} λ_{em} = 613 nm excitation spectra exactly in the same region as the observed ZnO band gap bands for the PVG excitation spectra (in depth analysis can be found in the supplementary material of Oliveira *et al.*[20]) suggests a ZnO → Eu^{III} energy transfer, and thus the very likely successful doping.

The following work by de Oliveira *et al.*[35] consolidated all the previous experience using the IDC method to design highly tailored NP for LED applications. The goal was to design NP as a possible solution to an ongoing challenge at the time: obtaining stable warm-white-light-emitting materials.[65-69] This required a precise combination of the different light-emitting species, as well as the structure in which they were to be arranged, to prevent the various

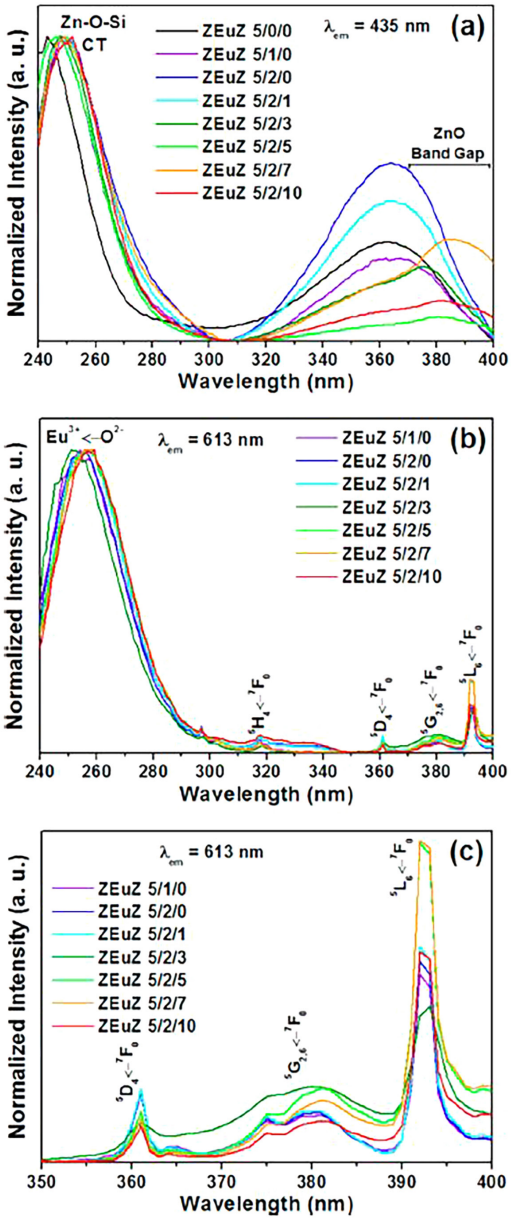

Figure 16. Excitation spectra of the PVG emission (λ_{em} = 435 nm) and most intense Eu^{III} emission ($^5D_0 \rightarrow {}^7F_2$, λ_{em} = 613 nm) obtained for ZnO@ZnO:Eu^{III}@ZnO samples, showing energy transfers from Zn–O–Si groups and ZnO to PVG, and possibly from ZnO to Eu^{III} (380-400 nm region) (reproduced with permission from reference 20, Copyright 2015, American Chemical Society).

possible effects occurring between the different involved species, such as energy transfers and non-radiative relaxation, from interfering with the desired result.

To reach this goal, the full potential of the IDC method was explored. The commercially available PVG was used as a porous host to control nanoparticle growth and size. ZrO_2 was selected as oxide host for its high chemical and thermal resistances, as well as good solubility for large interstitial species such as Ln^{III} ions. On that basis, for a precise control of luminescence, lanthanide ions Eu^{III} and

Tb^{III} were chosen as dopants to obtain red and green light emission, complementing the native-defect blue-emission from PVG. As a silica-based glass, however, the presence of Si–OH groups on PVG's internal surface presented both an advantage and a disadvantage, since –OH groups are a well-known source of non-radiative deactivation of Ln-based phosphors, especially of Eu^{III}. For this, a thin layer of ZnO was coated on the PVG's internal pore surface, based on the previous work by Oliveira *et al*.[20] Another effect to be prevented was the energy transfer between Tb^{III} and Eu^{III}. Considering their overall relative proximity inside a < 5 nm nanoparticle, the best strategy proved to be the physical separation between them through interstitial layers of pure oxide. Finally, tailoring the specific number of doped and pure layers allowed the fine-tuning of the light emission of the nanoparticles (Figure 17). In Figure 17 it is also clear to see the role that the nanostructure plays on the material performance, where the absence of pure layers in-between lead to $Eu^{III} \rightarrow Tb^{III}$ energy transfers occurring, the extreme case being when both are mixed for every layer (Figure 17f). The reader is referred to de Oliveira *et al*.[35] work for the in-depth analysis regarding the tuning of the light emission properties via the composition and nanostructure of the NP in these systems.

Herein we presented the metal oxide-based NP-porous host chemically integrated systems developed using the IDC method. This method provided a combined solution for synthesizing chemically integrated systems where < 10 nm NP may be stabilized, while also allowing control over their growth, composition and in some cases of their crystal phase. The use of a porous host also opened the doors for further exploiting the contribution of another component in the chemically integrated systems, for example where pores could function as nanoreactors for catalysis, or where a functional surface could be applied to prevent luminescence suppression effects over doped NP.

5. Conclusions

In this review we went through the research history of the synthesis of tailored chemically integrated systems composed of metal oxide nanoparticles grown inside porous matrices using the method of IDC. This layer-by-layer growth method combined with the pore structure size limitations allowed the fine tuning of the nanoparticle size, shape, crystalline phase and nanostructure through their hierarchical construction. The number and composition of the IDC layers allowed the tailoring of nanoparticle properties, such as the band gap energy or Raman absorption bands through quantum confinement effects, the fine control of the material's light emission through the number of doped layers and their order within the nanoparticles, as well as the construction of core@shell nanoparticles. This fine control of properties enabled the

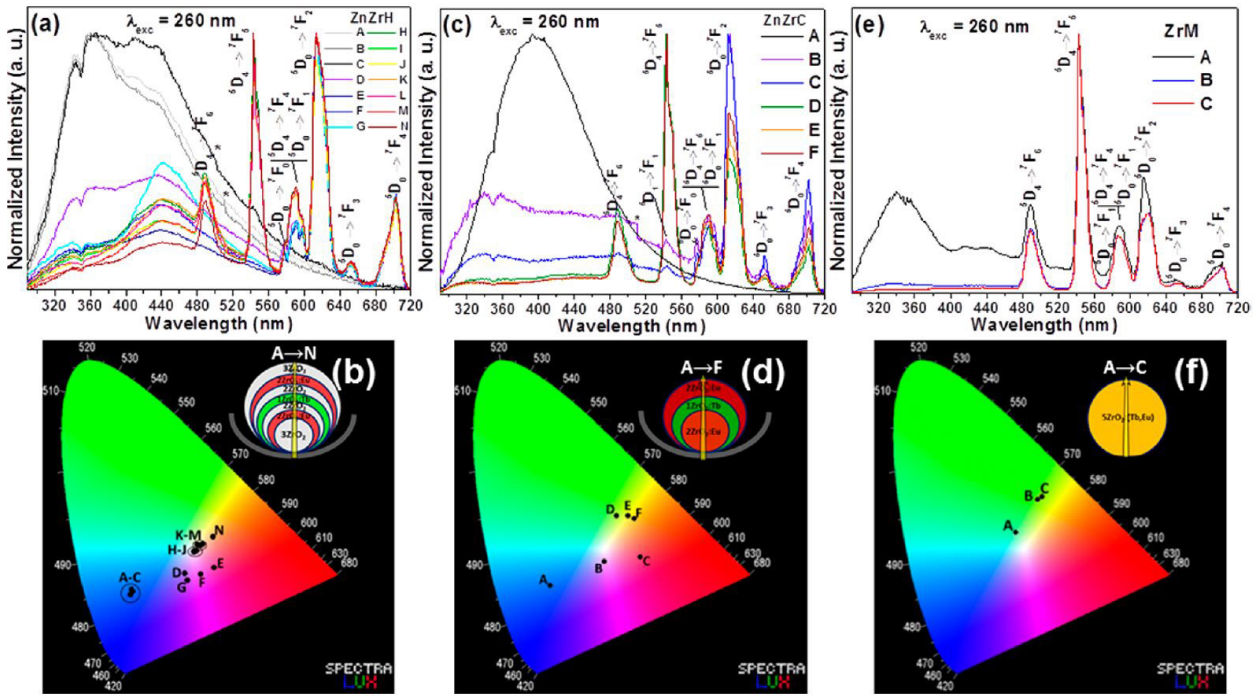

Figure 17. Emission spectra and corresponding CIE diagrams obtained for the Ln^{III}-doped ZrO_2 nanoparticles synthesized inside ZnO-coated PVG with varying layered compositions: (a,b) ZnZrH: with every Ln^{III}-doped layer separated by pure ZrO_2 layers; (c,d) ZnZrC: without pure ZrO_2 layers; ZrM: without ZnO coating and with both dopants (Eu^{III} and Tb^{III}) mixed for every IDC (reproduced with permission from reference 35, Copyright 2017, American Chemical Society).

synthesis of chemically integrated systems for applications in: catalysis, where NP stabilization in a different crystal structure as the obtained for bulk, as well as with very small sizes due to the porous host stabilization, presented the highest activity for photocatalysis due to the much higher surface area, even with the increased optical band gap; magnetic nanoparticles presented a special core@shell structure with different magnetic behaviors for core and shell; and for light emission the role of the hierarchical nanostructure of the nanoparticles played a pivotal role in the NP performance for white light emission. We believe this method still has a lot of unexplored potential for the scientific community, and this series of studies have shown there can be endless possibilities in terms of metal oxide combinations and hierarchical nanostructure designs for a variety of applications. A couple examples would be: multi-oxide hierarchical structures containing 3 or more oxides of interest for example in catalysis, which combined with specific metallic NP could generate chemically integrated systems with special performance; or the assembly of hierarchical metal-oxide NP with multifunctional pollutant degradation potential, where each layer could be responsible for a given set of pollutant molecules.

Acknowledgments

The authors gratefully acknowledge the financial support provided by the CNPq, FAPESP, CAPES and INCT/INOMAT (National Institute of Science Technology in Complex Functional Materials). Contributions from the Brazilian Center for Research in Energy and Materials (CNPEM), Brazilian Synchrotron Light Laboratory (LNLS), Brazilian Nanotechnology National Laboratory (LNNano), Laboratory of Molecular Spectroscopy (IQ-USP), Multiuser Laboratory of Advanced Optical Spectroscopy (LMEOA/IQ-UNICAMP) analyses are also gratefully acknowledged. This is a contribution of the National Institute of Science and Technology in Complex Functional Materials.

This work is dedicated to Professor Oswaldo Luiz Alves from the Institute of Chemistry, UNICAMP, a recognized and enthusiastic Professor/Researcher of the Solid State Chemistry and Nanoscience fields who suddenly and prematurely passed away on July 10th, 2021. The authors would like to acknowledge the immeasurable contribution that Prof Oswaldo Luiz Alves made not only to science, but to the lives and welfare of those that, in one way or another, could benefit from his work, wisdom and unyielding will.

Author Contributions

All the authors cooperated in the formal analysis, writing, reviewing, and editing of the original draft. C. S. O. and I. O. M. cooperated in the conceptualization and final revision of the manuscript; C. S. O. and I. O. M. edited the final version of the manuscript.

Cristine S. de Oliveira *holds a bachelor's degree in Pure and Applied Chemistry (2010), a master's degree in Chemistry (2013) and a PhD in Sciences (2017) from University of Campinas (UNICAMP). She then continued at UNICAMP for a post-doc until 2018, when she left to Germany for a post-doc at the Martin-Luther-University Halle-Wittenberg until 2020, and then continued her previous research at UNICAMP from 2021 until 2022 as a collaborating researcher. She then moved to the private sector in Germany, having led a laboratory for Corona diagnostics from 2022 until 2023. She currently works in a company in the sector of battery development. Dr Cristine has experience in the design, synthesis and advanced characterization of chemically integrated materials and nanomaterials for applications in light emission, catalysis, sensing, and environmental applications.*

Fernando A. Sigoli *holds a bachelor's degree in Chemistry (1993), a master's in Chemistry (1997) and PhD in Chemistry (2001) from the State University of São Paulo (UNESP). He has worked in the private sector in the United States from 2001 to 2005 as researcher, manager of research and development (R&D) of photonic devices. After that period, he returned to Brazil for a post-doc at the Institute of Chemistry at UNESP (2005-2006). He joined University of Campinas (UNICAMP) in 2006 as a Doctor Professor. Since 2013, he is an Associate Professor at the Institute of Chemistry of the UNICAMP. Prof Sigoli has experience in the field of Chemistry, with emphasis on Inorganic Chemistry in the preparation of lanthanide-doped nanomaterials and functionalized photoluminescent complexes applied to optical probes.*

Italo O. Mazali *holds a bachelor's degree in Chemistry with Technological Attributions (1994) and a master's degree in Chemistry (1997) from São Paulo State University (UNESP) and a PhD in Chemistry from University of Campinas (UNICAMP) (2001). He is currently a Full*

Professor at the Institute of Chemistry (UNICAMP). Prof Mazali has experience on synthesis with control of particles size and morphology of semiconductors oxides (magnetic, optical and catalytic properties) and noble metal nanoparticles (SERS applications); relationship between size, morphology and property, synergistic effect on core-shell nanoparticles; development of a methodology for the characterization of multicomponent nanostructured materials.

References

1. Khalil, M.; Kadja, G. T. M.; Ilmi, M. M.; *J. Ind. Eng. Chem.* **2021**, *93*, 78. [Crossref]
2. Astruc, D.; *Chem. Rev.* **2020**, *120*, 461. [Crossref]
3. Ramos, A. P.; Cruz, M. A. E.; Tovani, C. B.; Ciancaglini, P.; *Biophys. Rev.* **2017**, *9*, 79. [Crossref]
4. Shin, M. D.; Shukla, S.; Chung, Y. H.; Beiss, V.; Chan, S. K.; Ortega-Rivera, O. A.; Wirth, D. M.; Chen, A.; Sack, M.; Pokorski, J. K.; Steinmetz, N. F.; *Nat. Nanotechnol.* **2020**, *15*, 646. [Crossref]
5. Willner, M. R.; Vikesland, P. J.; *J. Nanobiotechnol.* **2018**, *16*, 95. [Crossref]
6. Shah, M. A.; Pirzada, B. M.; Price, G.; Shibiru, A. L.; Qurashi, A.; *J. Adv. Res.* **2022**, *38*, 55. [Crossref]
7. Pomerantseva, E.; Bonaccorso, F.; Feng, X.; Cui, Y.; Gogotsi, Y.; *Science* **2019**, *366*, 8285. [Crossref]
8. Wang, H.; Liang, X.; Wang, J.; Jiao, S.; Xue, D.; *Nanoscale* **2020**, *12*, 14. [Crossref]
9. Kim, T.-Y.; Kim, M. G.; Lee, J.-H.; Hur, H.-G.; *Front. Microbiol.* **2018**, *9*, 2817. [Crossref]
10. Guerra, F. D.; Attia, M. F.; Whitehead, D. C.; Alexis, F.; *Molecules* **2018**, *23*, 1760. [Crossref]
11. Beni, A. A.; Jabbari, H.; *Results Eng.* **2022**, *15*, 100467. [Crossref]
12. The Nobel Prize in Chemistry 2023, https://www.nobelprize.org/prizes/chemistry/2023/summary/, accessed in May 2024.
13. Rostami, S.; Ghaffarkhah, A.; Isari, A. A.; Hashemi, S. A.; Arjmand, M.; *Mater. Adv.* **2023**, *4*, 2698. [Crossref]
14. Ouhenia-Ouadahi, K.; Yasukuni, R.; Yu, P.; Laurent, G.; Pavageau, C.; Grand, J.; Guérin, J.; Léaustic, A.; Félidj, N.; Aubard, J.; Nakatani, K.; Métivier, R.; *Chem. Commun.* **2014**, *50*, 7299. [Crossref]
15. Li, W.; Wang, C.; Lu, X.; *J. Mater. Chem. A* **2021**, *9*, 3786. [Crossref]
16. Chen, Z.; Wu, C.; Yuan, Y.; Xie, Z.; Li, T.; Huang, H.; Li, S.; Deng, J.; Lin, H.; Shi, Z.; Li, C.; Hao, Y.; Tang, Y.; You, Y.; Al-Hartomy, O. A.; Wageh, S.; Al-Sehemi, A. G.; Lu, R.; Zhang, L.; Lin, X.; He, Y.; Zhao, G.; Li, D.; Zhang, H.; *J. Nanobiotechnol.* **2023**, *21*, 141. [Crossref]
17. Zhao, G.; Yang, F.; Chen, Z.; Liu, Q.; Ji, Y.; Zhang, Y.; Niu, Z.; Mao, J.; Bao, X.; Hu, P.; Li, Y.; *Nat. Commun.* **2017**, *8*, 14039. [Crossref]
18. Mazali, I. O.; Alvez, O. L.; *J. Phys. Chem. Solids* **2005**, *66*, 37. [Crossref]
19. Corrêa, D. N.; e Silva, J. M. S.; Santos, E. B.; Sigoli, F. A.; Souza Filho, A. G.; Mazali, I. O.; *J. Phys. Chem. C* **2011**, *115*, 10380. [Crossref]
20. Oliveira, C. S.; Bettini, J.; Sigoli, F. A.; Mazali, I. O.; *Cryst. Growth Des.* **2015**, *15*, 5246. [Crossref]
21. Thanh, N. T.; Maclean, N.; Mahiddine, S.; *Chem. Rev.* **2014**, *114*, 7610. [Crossref]
22. Mazali, I. O.; Souza Filho, A. G.; Viana, B. C.; Mendes Filho, J.; Alves, O. L.; *J. Nanopart. Res.* **2006**, *8*, 141. [Crossref]
23. Santos, E. B.; e Silva, J. M. S.; Mazali, I. O.; *Vib. Spectrosc.* **2010**, *54*, 89. [Crossref]
24. Strauss, M.; Pastorello, M.; Sigoli, F. A.; e Silva, J. M. S.; Mazali, I. O.; *Appl. Surf. Sci.* **2014**, *319*, 151. [Crossref]
25. Cangussu, D.; Nunes, W. C.; Corrêa, H. L. S.; Macedo, W. A. A.; Knobel, M.; Alves, O. L.; Souza Filho, A. G.; Mazali, I. O.; *J. Appl. Phys.* **2009**, *105*, 013901. [Crossref]
26. Mazali, I. O.; Viana, B. C.; Alves, O. L.; Mendes Filho, J.; Souza Filho, A. G.; *J. Phys. Chem. Solids* **2007**, *68*, 622. [Crossref]
27. Mazali, I. O.; Romano, R.; Alves, O. L.; *Thin Solid Films* **2006**, *495*, 64. [Crossref]
28. Oliveira, M. M.: *Obtenção de Nanocompósitos de Óxidos Semicondutores Inseridos em Vidro Poroso Vycor via Decomposição de Precursores Metalorgânicos*; MSc Dissertation, University of Campinas, Campinas, Brazil, 2000. [Link] accessed in April 2024.
29. Carneiro, N. M.; Nunes, W. C.; Borges, R. P.; Godinho, M.; Fernandez-Outon, L. E.; Macedo, W. A. A.; Mazali, I. O.; *J. Phys. Chem. C* **2010**, *114*, 18773. [Crossref]
30. Santos, E. B.; e Silva, J. M. S.; Sigoli, F. A.; Mazali, I. O.; *J. Nanopart. Res.* **2011**, *13*, 5909. [Crossref]
31. Strauss, M.; Destefani, T. A.; Sigoli, F. A.; Mazali, I. O.; *Cryst. Growth Des.* **2011**, *11*, 4511. [Crossref]
32. e Silva, J. M. S.; Strauss, M.; Maroneze, C. M.; Souza, E. R.; Gushikem, Y.; Sigoli, F. A.; Mazali, I. O.; *J. Mater. Chem.* **2011**, *21*, 15678. [Crossref]
33. e Silva, J. M. S.; Pastorello, M.; Strauss, M.; Maroneze, C. M.; Sigoli, F. A.; Gushikem, Y.; Mazali, I. O.; *RSC Adv.* **2012**, *2*, 5390. [Crossref]
34. Kalinke, L. H. G.; Stumpf, H. O.; Mazali, I. O.; Cangussu, D.; *Mater. Res. Bull.* **2015**, *70*, 743. [Crossref]
35. de Oliveira, C. S.; Bettini, J.; Sigoli, F. A.; Mazali, I. O.; *Cryst. Growth Des.* **2017**, *17*, 5398. [Crossref]
36. Kocsis, G.; Szabó-Bárdos, E.; Fónagy, O.; Farsang, E.; Juzsakova, T.; Jakab, M.; Pekker, P.; Kovács, M.; Horváth, O.; *Molecules* **2022**, *27*, 8041. [Crossref]
37. Chu, J.; Sun, Y.; Han, X.; Zhang, B.; Du, Y.; Song, B; Xu, P.; *ACS Appl. Mater. Interfaces* **2019**, *11*, 18475. [Crossref]

38. Sampaio, M. J.; Yu, Z.; Lopes, J. C.; Tavares, P. B.; Silva, C. G.; Liu, L.; Faria, J. L.; *Sci. Rep.* **2021**, *11*, 21306. [Crossref]
39. Oi, L. E.; Choo, M.-Y.; Lee, H. V.; Oong, H. C.; Hamid, S. B. A.; Juan, J. C.; *RSC Adv.* **2016**, *6*, 108741. [Crossref]
40. Macino, M.; Barnes, A. J.; Althahban, S. M.; Qu, R.; Gibson, E. K.; Morgan, D. J.; Freakley, S. J.; Dimitratos, N.; Kiely, C. J.; Gao, X.; Beale, A. M.; Bethell, D.; He, Q.; Sankar, M.; Hutchings, G. J.; *Nat. Catal.* **2019**, *2*, 873. [Crossref]
41. Zhang, H.; Zuo, S.; Qiu, M.; Wang, S.; Zhang, Y.; Zhang, J.; Lou, X. W.; *Sci. Adv.* **2020**, *6*, eabb9823. [Crossref]
42. Richter, H.; Wang, Z. P.; Ley, L.; *Solid State Commun.* **1981**, *39*, 625. [Crossref]
43. Zhou, J.; Guo, R.-t.; Zhang, X.-f.; Liu, Y.-z.; Duan, C.-p.; Wu, G.-l.; Pan, W.-g.; *Energy Fuels* **2021**, *35*, 2981. [Crossref]
44. Liyanage, A. D.; Perera, S. D.; Tan, K., Chabal, Y.; Balkus Jr., K. J.; *ACS Catal.* **2014**, *4*, 577. [Crossref]
45. Luo, S.; Barrio, L.; Nguyen-Phan, T.-D.; Vovchok, D.; Johnston-Peck, A. C.; Xu, W.; Stach, E. A.; Rodriguez, J. A.; Senanayake, S. D.; *J. Phys. Chem. C* **2017**, *121*, 6635. [Crossref]
46. Wu, L.; Fang, S.; Ge, L.; Han, C.; Qiu, P.; Xin, Y.; *J. Hazard Mater.* **2015**, *300*, 93. [Crossref]
47. Jiang, D.; Wang, W.; Sun, S.; Zhang, L.; Zheng, Y.; *ACS Catal.* **2015**, *5*, 613. [Crossref]
48. Spanier, J. E.; Robinson, R. D.; Zhang, F.; Chan, S.-W.; Herman, I. P.; *Phys. Rev. B* **2001**, *64*, 245407. [Crossref]
49. Coduri, M.; Masala, P.; Del Bianco, L.; Spizzo, F.; Ceresoli, D.; Castellano, C.; Cappelli, S.; Oliva, C.; Checchia, S.; Allieta, M.; Szabo, S. V.; Schlabach, S.; Hagelstein, M.; Ferrero, C.; Scavini, M.; *Nanomaterials* **2020**, *10*, 867 [Crossref]
50. Cao, D.; Li, H.; Pan, L.; Li, J.; Wang, X.; Jing, P.; Cheng, X.; Wang, W.; Wang, J.; Liu, Q.; *Sci. Rep.* **2016**, *6*, 32360. [Crossref]
51. Wu, W.; Xiao, X. H.; Zhang, S. F.; Peng, T. C.; Zhou, J.; Ren, F.; Jiang, C. Z.; *Nanoscale Res. Lett.* **2010**, *5*, 1474. [Crossref]
52. Guivar, J.; Martínez, A.; Anaya, A.; Valladares, L.; Félix, L.; Dominguez, A.; *Adv. Nanopart.* **2014**, *3*, 114. [Crossref]
53. Tadic, M.; Nikolic, D.; Panjan, M.; Blake, G. R.; *J. Alloys Compd*. **2015**, *647*, 1061. [Crossref]
54. Janus, W.; Ślęzak, T.; Ślęzak, M.; Szpytma, M.; Dróżdż, P.; Nayyef, H.; Mandziak, A.; Wilgocka-Ślęzak, D.; Zając, M.; Jugovac, M.; Menteş, T. O.; Locatelli, A.; Kozioł-Rachwał, A.; *Sci. Rep.* **2023**, *13*, 4824. [Crossref]
55. Jafari, A.; Jahromi, S. P.; Boustani, K.; Goh, B. T.; Huang, N. M.; *J. Magn. Magn. Mater.* **2019**, *469*, 383. [Crossref]
56. Al Boukhari, J.; Khalaf, A.; Awad, R.; *Appl. Phys. A* **2020**, *126*, 74. [Crossref]
57. Swiatkowska-Warkocka, Z.; Pyatenko, A.; Shimizu, Y.; Perzanowski, M.; Zarzycki, A.; Jany, B. R.; Marszalek, M.; *Nanomaterials* **2018**, *8*, 790. [Crossref]
58. Mukherjee, S.; Katea, S. N.; Rodrigues, E. M.; Segre, C. U.; Hemmer, E.; Broqvist, P.; Rensmo, H.; Westin, G.; *Small* **2023**, *19*, 2203331. [Crossref]
59. Haj-Hmeidi, Y.; Röder, R.; Cammi, D.; Ronning, C.; *Nanotechnology* **2019**, *30*, 095201. [Crossref]
60. Aneesh, P. M.; Jayaraj, M. K.; *Bull. Mater. Sci.* **2010**, *33*, 227. [Crossref]
61. Jiang, N.; Ye, S.; Qiu, J.; *J. Appl. Phys.* **2010**, *108*, 083535. [Crossref]
62. Shannon, R. D.; Prewitt, C. T.; *Acta Crystallogr., Sect. B: Struct. Sci., Cryst. Eng. Mater.* **1969**, *B25*, 925. [Crossref]
63. Lima, S. A. M.; Sigoli, F. A.; Davolos, M. R.; *J. Solid State Chem.* **2003**, *171*, 287. [Crossref]
64. Liu, Y.; Luo, W.; Li, R.; Liu, G.; Antonio, M. R.; Chen, X.; *J. Phys. Chem. C* **2008**, *112*, 686. [Crossref]
65. Oh, J. H.; Yang, S. J.; Do, Y. R.; *Light: Sci. Appl.* **2014**, *3*, e141. [Crossref]
66. Kuse, Y.; Ogawa, K.; Tsuruma, K.; Shimazawa, M.; Hara, H.; *Sci. Rep.* **2014**, *4*, 5223. [Crossref]
67. Rai, M.; Kaur, G.; Singh, S. K.; Rai, S. B.; *Dalton Trans.* **2015**, *44*, 6184. [Crossref]
68. Borik, M.; Kulebyakin, A.; Kyashkin, V.; Larina, N.; Lomonova, E.; Milovich, F.; Myzina, V.; Nezhdanov, A.; Ryabochkina, P.; Tabachkova, N.; Chernov, E.; *Materials* **2022**, *15*, 7722. [Crossref]
69. Lovisa, L. X.; Andrés, J.; Gracia, L.; Li, M. S.; Paskocimas, C. A.; Bornio, M. R. D.; Araujo, V. D.; Longo, E.; Motta, F. V.; *J. Alloys Compd.* **2017**, *695*, 3094. [Crossref]

Submitted: January 26, 2024
Published online: May 20, 2024